Monthly Notices of the ROYAL ASTRONOMICAL SOCIETY

MNRAS **539,** 1908–1921 (2025) https://doi.org/10.1093/mnras/staf565
Advance Access publication 2025 April 7

Multipeaked non-thermal light curves from magnetar-powered gamma-ray bursts

Conor M. B. Omand [1]★ Nikhil Sarin [2,3] and Gavin P. Lamb [1]

[1]*Astrophysics Research Institute, Liverpool Jo , , Liverpool Science Park IC2, 146 Brownlow Hill, Liverpool L3 5R, UK*
[2]*The Oskar Klein Centre, Department of Physics, Stockholm University, AlbaNova, SE-106 91 Stockholm, Sweden*
[3]*Nordita, Stockholm University and KTH Royal Institute of Technology Hannes Alfvéns väg 12, SE-106 91 Stockholm, Sweden*

Accepted 2025 March 27. Received 2025 March 6; in original form 2024 December 16

ABSTRACT

Binary neutron star mergers and collapsing massive stars can both create millisecond magnetars. Such magnetars are candidate engines to power gamma-ray bursts (GRBs). The non-thermal light curve of the resulting transients can exhibit multiple components, including the GRB afterglow, pulsar wind nebula (PWN), and ejecta afterglow. We derive the time-scales for the peak of each component and show that the PWN is detectable at radio frequencies, dominating the emission for ∼6 yr for supernova/long GRBs (SN/LGRBs) and ∼ 100 d for kilonova/short GRBs (KN/SGRBs) at 1 GHz, and ∼1 yr for SN/LGRBs and ∼ 15 d for KN/SGRBs at 100 GHz. The PWN emission has an exponential, frequency-dependent rise to peak that cannot be replicated by an ejecta afterglow. We show that PWNe in SN/LGRBs can be detected out to $z \sim 0.06$ with current instruments and $z \sim 0.3$ with next-generation instruments and PWNe in KN/SGRBs can be detected out to $z \sim 0.3$ with current instruments and $z \sim 1.5$ with next-generation instruments. We find that the optimal strategy for detecting PWNe in these systems is a multiband, high cadence radio follow-up of nearby KN/SGRBs with an X-ray plateau or extended prompt emission from 10 to 100 d post-burst.

Key words: radiation mechanisms: non-thermal – stars: magnetars – (transients:) gamma-ray bursts – (transients:) neutron star mergers – transients: supernovae.

1 INTRODUCTION

Gamma-ray bursts (GRBs) are short flashes of high-energy radiation formed within relativistic jets (Piran 2004; Gehrels & Mészáros 2012; Zhang 2018). They are typically divided into two categories based on the duration of their prompt emission, with short GRBs (SGRBs) having a duration of $T_{90} \lesssim 2$ s and long GRBs (LGRBs) having a duration of $T_{90} \gtrsim 2$ s (Kouveliotou et al. 1993), where T_{90} is the time-scale over which 90 per cent of the background-subtracted counts are observed. The two GRB classes also show differences in their spectra, with SGRBs typically showing harder spectra than LGRBs (Kouveliotou et al. 1993). This dichotomy supports the idea that these distinct GRB classes arise from different progenitor channels, with SGRBs originating from compact object mergers (Lattimer & Schramm 1976; Blinnikov et al. 1984; Eichler et al. 1989) and LGRBs originating from the collapse of massive stars (MacFadyen & Woosley 1999; MacFadyen, Woosley & Heger 2001). There is observational evidence that supports this distinction; LGRBs have been associated with supernovae (SNe; e.g. Gendre et al. 2013; Nakauchi et al. 2013; Levan et al. 2014; Cano et al. 2017), and several SGRBs associated with kilonovae (KNe; e.g. Tanvir et al. 2013; Yang et al. 2015; Jin et al. 2016; Lamb et al. 2019b; Jin et al. 2020; Fong et al. 2021; Zhou et al. 2023; Zhu et al. 2023), including the SGRB GRB170817A accompanying the binary neutron star (BNS) merger that produced GW170817 (Abbott et al. 2017a). However, two recent LGRBs have been inferred to have originated from BNS mergers due to emission resembling that of a KN (Rastinejad et al. 2022; Levan et al. 2024), casting some doubt on the robustness of this classification scheme.

Most models for launching relativistic jets that produce GRBs require angular momentum and energy from a compact object – accretion disc system. The compact object can either be a black hole or a highly magnetized neutron star, known as a magnetar (Duncan & Thompson 1992). For black holes, the energy can be extracted from the black hole spin (Blandford & Znajek 1977) or accretion disc (Blandford & Payne 1982) via a twisted magnetic field, or neutrino winds from the accretion disc (e.g. Popham, Woosley & Fryer 1999). While magnetars can launch jets via similar processes, they can also launch jets from a magnetorotational mechanism with strong dipolar or toroidal fields (Mösta et al. 2020; Bugli, Guilet & Obergaulinger 2021), or from strong propeller-driven outflows (Illarionov & Sunyaev 1975; Lovelace, Romanova & Bisnovatyi-Kogan 1999; Romanova et al. 2005).

When the relativistic jet sweeps up material and starts to decelerate, a broad-band synchrotron and inverse Compton GRB afterglow is emitted (Paczynski & Rhoads 1993; Sari, Piran & Narayan 1998; Piran 2004; Zhang & Mészáros 2004; Zhang et al. 2006; MAGIC Collaboration et al. 2019). The temporal light curve of this afterglow will be dominated by the jet core for on-axis observers and will

★ E-mail: c.m.omand@ljmu.ac.uk

depend on the wider structure of the jet for off-axis observers (Granot et al. 2002; Rossi, Lazzati & Rees 2002). While the afterglow emission is mostly predicted to rise and fall as power laws (Sari et al. 1998), several other phenomena have been detected in the afterglow emission. One of these phenomena are X-ray plateaus, where the flux of the X-ray afterglow transitions from an initial steep decay, to a very shallow decay or plateau, back to a steep decay (Nousek et al. 2006; O'Brien et al. 2006; Rowlinson et al. 2013; Dainotti et al. 2017). This has been suggested to be due to energy injection from a central magnetar (Troja et al. 2007; Rowlinson et al. 2013; Gompertz, O'Brien & Wynn 2014; Stratta et al. 2018; Sarin, Lasky & Ashton 2019). Another GRB phenomenon potentially linked to a magnetar central engine is extended emission (Metzger, Quataert & Thompson 2008; Bucciantini et al. 2012; Gompertz et al. 2013; Gompertz et al. 2014; Gibson et al. 2017), where the prompt GRB emission is followed by a lower luminosity signal that can be several times longer than the prompt emission and extends to softer energies (Norris & Bonnell 2006; Bostancı, Kaneko & Göğüş 2013; Kaneko et al. 2015).

The wind from the spin-down of a rotating neutron star will also produce a pulsar wind nebula (PWN) on the interior of the ejecta that is a broad-band synchrotron and inverse Compton emitter. The thermalization of PWN emission in the ejecta is thought to power a number of transients, including superluminous supernovae (SLSNe; Nicholl, Guillochon & Berger 2017; Kangas et al. 2022; West et al. 2023; Gkini et al. 2024; Gomez et al. 2024) and some broad-line SN-Ic (SNe Ic-BL) (Mazzali et al. 2014; Greiner et al. 2015; Wang et al. 2017; Omand & Sarin 2024). The PWN can also be detected in radio (Murase et al. 2015; Omand, Kashiyama & Murase 2018; Eftekhari et al. 2019; Law et al. 2019; Mondal et al. 2020; Eftekhari et al. 2021). It can also cause an infrared excess by heating up dust in the ejecta (Omand, Kashiyama & Murase 2019; Chen et al. 2021; Sun, Xiao & Li 2022), change the spectrum by ionizing the ejecta (Chevalier & Fransson 1992; Jerkstrand et al. 2017; Omand & Jerkstrand 2023; Dessart 2024), and cause polarization signals by expanding the ejecta asymmetrically (Inserra et al. 2016; Saito et al. 2020; Poidevin et al. 2022; Pursiainen et al. 2022; Poidevin et al. 2023; Pursiainen et al. 2023). The PWN can also cause instabilities in the ejecta (Chen, Woosley & Sukhbold 2016; Suzuki & Maeda 2017, 2021) that results in a filamentary ejecta structure similar to the Crab Nebula (Clark et al. 1983; Bietenholz et al. 1991; Temim et al. 2006; Omand, Sarin & Temim 2025).

The ejecta from a transient accompanying a GRB, an SN or a KN, can produce its own afterglow once it sweeps up enough mass to decelerate the ejecta. X-ray observations of GRB170817A have shown tentative evidence for a re-brightening of the afterglow at late times potentially consistent with this scenario (Hajela et al. 2022; Troja et al. 2022). A few SNe have been detected in radio at late times (e.g. van Dyk et al. 1994; Gaensler et al. 1997; Corsi et al. 2023; Kool et al. 2023; Margutti et al. 2023) and X-ray (e.g. Chevalier & Fransson 1994; Dwarkadas 2014; Bochenek et al. 2018), and some at much earlier times when dense circumstellar material (CSM) surrounds the progenitor (e.g. Smith et al. 2008; Fransson et al. 2014; Drout et al. 2016).

Magnetar-driven GRB systems should produce non-thermal emission from a GRB afterglow, PWN, and SN/KN afterglow (we refer to this as an ejecta afterglow), as well as thermal emission from the magnetar-heated ejecta. The time-scale for these three non-thermal mechanisms can be significantly different, leading to the potential of detecting all three components separately. The GRB and ejecta afterglow both arise when the jet and ejecta sweep up an amount of mass comparable to their own mass divided by their Lorentz factor (Rees & Meszaros 1992; Sari & Piran 1995), but the jet is much faster and less massive, leading to the GRB afterglow peaking much earlier. The peak of the PWN emission is set by the opacity of the ejecta, which can vary greatly across bands due to the different absorption processes involved at different energies. However, for most energies, the PWN will peak sometime in between the GRB afterglow and ejecta afterglow, leading to a distinct third component. Previous modelling studies of magnetar-driven GRBs or SN/GRBs have not considered all three components (e.g. Murase et al. 2018; Sarin et al. 2022; Kusafuka, Matsuoka & Sawada 2025), and previous observations searching for multiple components have only led to upper limits (e.g. Schroeder et al. 2020).

Here, we examine the emission for each component and show the multipeaked non-thermal light curves that can result from such systems. In Section 2, we derive the scaling relations and fiducial time-scales for the three components. In Section 3, we show the resulting light curves in radio and X-ray, and show that the magnetar signal cannot be reproduced by an ejecta afterglow. In Section 4, we discuss strategies for observation, caveats and uncertainties of our approach, and analyze a few notable GRBs. Finally, in Section 5, we summarize our findings.

2 ANALYTIC TIME-SCALE ESTIMATES

Here, we estimate the time-scales of the peaks of each non-thermal component using simple analytic scalings at radio and X-ray frequencies. The fiducial time-scales for each component in both the KN and SN scenarios are summarized in Table 1.

2.1 GRB afterglow

We estimate the peak time-scale for an on-axis afterglow using the standard closure relations (Sari et al. 1998). We assume a fully adiabatic shock and that the afterglow is in the slow-cooling regime. We also assume that the density of the ambient medium is constant. The time-scales where the cooling frequency ν_c and the frequency at the minimum electron acceleration ν_m cross the observed frequency ν are

$$t_c \approx 7.3 \left(\frac{\epsilon_B}{0.01}\right)^{-3} \left(\frac{E_{\rm jet}}{10^{52}\ {\rm erg}}\right)^{-1} \left(\frac{n_{\rm CSM}}{1\ {\rm cm}^{-3}}\right)^{-2} \left(\frac{\nu}{10^6\ {\rm GHz}}\right)^{-2}\ {\rm d}, \quad (1)$$

$$t_m \approx 10 \left(\frac{\epsilon_B}{0.01}\right)^{1/3} \left(\frac{\epsilon_e}{0.1}\right)^{4/3} \left(\frac{E_{\rm jet}}{10^{52}\ {\rm erg}}\right)^{1/3} \left(\frac{\nu}{10^6\ {\rm GHz}}\right)^{-2/3}\ {\rm min}, \quad (2)$$

where ϵ_B and ϵ_e are the fractions of shock energy that go into magnetic field and leptons, respectively, $E_{\rm jet}$ is the energy of the jet, and $n_{\rm CSM}$ is the number density of the ambient medium. Whether the peak of the light curve is set by t_c or t_m is determined by which time-scale is shorter, which can be determined by the critical frequency

$$\nu_{\rm crit} \approx 1.8 \times 10^8 \left(\frac{\epsilon_B}{0.01}\right)^{-5/2} \left(\frac{\epsilon_e}{0.1}\right)^{-1} \left(\frac{E_{\rm jet}}{10^{52}\ {\rm erg}}\right)^{-1} \times \left(\frac{n_{\rm CSM}}{1\ {\rm cm}^{-3}}\right)^{-3/2}\ {\rm GHz}. \quad (3)$$

For $\nu > \nu_{\rm crit}$ (the high-frequency light curve), the peak occurs at t_c, while for $\nu < \nu_{\rm crit}$ (the low-frequency light curve), the peak occurs at t_m. $\nu = \nu_{\rm crit}$ at the critical time-scale is

$$t_{\rm crit} \approx 18 \left(\frac{\epsilon_B}{0.01}\right)^{2} \left(\frac{\epsilon_e}{0.1}\right)^{2} \left(\frac{E_{\rm jet}}{10^{52}\ {\rm erg}}\right) \left(\frac{n_{\rm CSM}}{1\ {\rm cm}^{-3}}\right)\ {\rm s} \quad (4)$$

This time-scale is much earlier than the time-scales we observe, and justifies our assumption of slow cooling.

Table 1. The peak time-scale of each non-thermal component at various radio and X-ray bands for our fiducial parameters. The parameters used for estimating the time-scales and the scaling relations for each value can be found in their respective sections.

Transient	Component	1 GHz	100 GHz	1 keV	100 keV
SN/LGRB	GRB afterglow	70 d	3 d	100 s	100 s
	PWN	10 yr	500 d	60 yr	100 d
	Ejecta afterglow	80 yr	80 yr	80 yr	80 yr
KN/SGRB	GRB afterglow	7 d	8 hours	20 s	20 s
	PWN	100 d	15 d	6 yr	2 d
	Ejecta afterglow	3 yr	3 yr	3 yr	3 yr

If these time-scales are shorter than the jet deceleration time-scale (Blandford & McKee 1976, 1977; Mészáros 2006)

$$t_{\rm dec,jet} = 100 \left(\frac{E_{\rm jet}}{10^{52}\ {\rm erg}}\right)^{1/3} \left(\frac{n_{\rm CSM}}{1\ {\rm cm}^{-3}}\right)^{-1/3} \left(\frac{\gamma_0}{100}\right)^{-8/3} {\rm s}, \quad (5)$$

where γ_0 is the initial Lorentz factor of the jet, then the light curve will peak at the deceleration time. For a typical observed LGRB jet with $\epsilon_e \sim 0.1$, $\epsilon_B \sim 0.01$, $E_{\rm jet} \sim 10^{52}$ erg, $\gamma_0 \sim 100$, and $n_{\rm CSM} \sim 1$ cm^{-3} (Wang et al. 2015; Atteia et al. 2017), the critical frequency is $\nu_{\rm crit} \sim 2 \times 10^8$ GHz ≈ 1 keV, and the peak time-scales in the radio bands are ~ 70 d at 1 GHz and around 3 d at 100 GHz, while in the X-ray bands they are set by the deceleration time, ~ 100 s. For a typical observed SGRB, with the same ϵ_e, ϵ_B, γ_0, and $n_{\rm CSM}$, but a lower jet energy of $E_{\rm jet} \sim 10^{50}$ erg (Fong et al. 2015), the critical frequency is $\nu_{\rm crit} \sim 2 \times 10^{11}$ GHz ≈ 100 keV, and the peak time-scales in the radio bands are ~ 7 d at 1 GHz and around 8 hours at 100 GHz, while in the X-ray bands they are set by the deceleration time, ~ 20 s.

For an afterglow viewed from off-axis, the peak will be delayed compared to the same afterglow viewed on-axis. For $\theta_{\rm obs} \gg \theta_{\rm jet}$, the peak time-scale will change $\propto \theta_{\rm obs}^{8/3}$, regardless of the angular structure of the jet[1] (Nakar, Piran & Granot 2002; Lamb & Kobayashi 2017; Ioka & Nakamura 2018; Xie, Zrake & MacFadyen 2018).

2.2 PWN

We estimate the peak time-scale for a PWN using the relations derived by the model in Appendix A. Due to the PWN emission being produced shortly after the explosion from the inside of the ejecta, the time-scale for the observed peak is set by when the optical depth of the ejecta in a specific band drops to unity. For radio emission, the key process is free–free absorption (FFA), although synchrotron self-absorption (SSA) can be key in certain regions of parameter space; for soft X-rays, it is photoelectric absorption; and for hard X-rays, it is Compton scattering.

Taking equations (A9), (A12), and (A13) for optical depth and solving for the time-scales where $\tau = 1$ gives

$$t_{\rm esc,ff} \approx 130 \left(\frac{M_{\rm ej}}{M_\odot}\right)^{2/5} \left(\frac{Y_{\rm fe}}{0.05}\right)^{2/5} \left(\frac{\bar{Z}}{10}\right)^{2/5} \left(\frac{v_{\rm ej}}{10^5\ {\rm km\ s}^{-1}}\right)^{-1} \left(\frac{\nu}{10\ {\rm GHz}}\right)^{-0.42} {\rm d}, \quad (6)$$

$$t_{\rm esc,pe} \approx 80 \left(\frac{M_{\rm ej}}{M_\odot}\right)^{1/2} \left(\frac{\bar{Z}}{10}\right) \left(\frac{v_{\rm ej}}{10^5\ {\rm km\ s}^{-1}}\right)^{-1} \left(\frac{h\nu}{10\ {\rm keV}}\right)^{-3/2} {\rm d}, \quad (7)$$

[1]This applies as long as the jet has a core-dominated structure.

$$t_{\rm esc,comp} \approx 10 \left(\frac{M_{\rm ej}}{M_\odot}\right)^{1/2} \left(\frac{Y_{\rm e}}{0.5}\right)^{1/2} \left(\frac{v_{\rm ej}}{10^5\ {\rm km\ s}^{-1}}\right)^{-1} \left(\frac{\sigma_{\rm KN}(\nu)}{\sigma_{\rm T}}\right)^{1/2} {\rm d}, \quad (8)$$

where $Y_{\rm fe}$ is the free electron fraction (defined in equation A11) within the ejecta, $\bar{Z}$ is the average atomic number of the ejected material, $v_{\rm ej}$ is the ejecta velocity, Y_e is the electron fraction within the ejecta, and $\sigma_{\rm KN}$ and σ_T are the Klein-Nishina and Thompson cross-sections, respectively.

For a fiducial GRB-SN with parameters chosen to be broadly consistent with observations (Taddia et al. 2019; Srinivasaragavan et al. 2024), the ejecta mass and velocity will be around 5 $M_\odot$ and 20 000 km s^{-1}, giving a total kinetic energy of $\sim 10^{52}$ erg. The ejecta is assumed to consist of singly ionized oxygen, which has $Y_{\rm e} \sim 0.5$, $\bar{Z} \sim 8$, and $Y_{\rm fe} \sim 1/16$. The assumption of oxygen ejecta is motivated by previous nucleosynthesis studies on GRB-SNe (e.g. Maeda et al. 2002) and the assumption of single-ionization is motivated by studies examining the ionization state of the ejecta in magnetar-driven SNe (Margalit et al. 2018; Omand & Jerkstrand 2023). Given these parameters, the peak time-scale is ~ 10 yr at 1 GHz, ~ 500 d at 100 GHz, ~ 60 yr at 1 keV, and ~ 100 d at 100 keV.

For our fiducial magnetar-driven KN, motivated by previous modelling efforts and numerical simulations (Yu, Zhang & Gao 2013; Siegel & Metzger 2017; Murase et al. 2018; Margalit & Metzger 2019; Metzger 2019; Sarin et al. 2022; Ai, Gao & Zhang 2025), the ejecta mass and velocity will be around 0.1 $M_\odot$ and $0.5c$, giving a total kinetic energy of $\sim 2 \times 10^{52}$ erg. The ejecta is assumed to have $Y_{\rm e} \sim 0.4$, $\bar{Z} \sim 40$, and $Y_{\rm fe} \sim 0.02$, which is broadly consistent with r-process nucleosynthesis calculations (Foucart et al. 2016; Roberts et al. 2017; Vlasov et al. 2017). Given these parameters, the peak time-scale is ~ 100 d at 1 GHz, ~ 15 d at 100 GHz, ~ 6 yr at 1 keV, and ~ 2 d at 100 keV.

2.3 Ejecta afterglow

The emission from the ejecta-CSM interaction will peak around the time when the ejecta sweeps up a mass comparable to itself, known as the ejecta deceleration time-scale. Following Nakar & Piran (2011) (see also Hotokezaka et al. 2016), a spherical outflow with energy $E_{\rm ej}$ and velocity $c\beta_0$ propagating into a medium of constant density $n_{\rm CSM}$ will begin to decelerate at a radius of

$$R_{\rm dec} \approx 10^{18} \left(\frac{E_{\rm ej}}{10^{52}\ {\rm erg}}\right)^{1/3} \left(\frac{n_{\rm CSM}}{1\ {\rm cm}^{-3}}\right)^{-1/3} \beta_0^{-2/3}\ {\rm cm} \quad (9)$$

on a time-scale of

$$t_{\rm dec,ejecta} = \frac{R_{\rm dec}}{c\beta_0} \approx 300 \left(\frac{E_{\rm ej}}{10^{52}\ {\rm erg}}\right)^{1/3} \left(\frac{n_{\rm CSM}}{1\ {\rm cm}^{-3}}\right)^{-1/3} \beta_0^{-5/3}\ {\rm d}. \tag{10}$$

$E_{\rm ej}$ is calculated from the initial kinetic energy $E_{\rm K}$ from the explosion/merger and the contribution from the magnetar, which depends of the spin-down luminosity and time-scale as well as the ejecta mass (for further discussion, see Suzuki & Maeda (2021) and Omand & Sarin (2024)). The peak time-scale can be longer if the observed frequency is below either the self-absorption frequency $\nu_{\rm ssa}$ or the synchrotron frequency at the minimum Lorentz factor ν_m at the deceleration time-scale. These frequencies have values

$$\nu_{\rm ssa} \approx 1 \left(\frac{E_{\rm ej}}{10^{49}\ {\rm erg}}\right)^{\frac{2}{3(4+p)}} \left(\frac{n_{\rm CSM}}{1\ {\rm cm}^{-3}}\right)^{\frac{14+3p}{6(4+p)}} \left(\frac{\epsilon_B}{0.1}\right)^{\frac{2+p}{2(4+p)}} \left(\frac{\epsilon_e}{0.1}\right)^{\frac{2(p-1)}{4+p}} \beta_0^{\frac{15p-10}{3(4+p)}}\ {\rm GHz} \tag{11}$$

$$\nu_m \approx 1 \left(\frac{n_{\rm CSM}}{1\ {\rm cm}^{-3}}\right)^{1/2} \left(\frac{\epsilon_B}{0.1}\right)^{1/2} \left(\frac{\epsilon_e}{0.1}\right)^{2} \beta_0^5\ {\rm GHz} \tag{12}$$

at $t_{\rm dec}$, where $p \sim 2.5$ is the index of the accelerated electrons ${\rm d}N/{\rm d}\gamma \propto \gamma^{-p}$. For a fiducial GRB SN ($E_{\rm ej} \sim 10^{52}$ erg, $\beta_0 \sim 0.06$, $n_{\rm CSM} \sim 1\ {\rm cm}^{-3}$, $\epsilon_B = \epsilon_e \sim 0.1$) and for ejecta from a magnetar-driven KN ($E_{\rm ej} \sim 10^{52}$ erg, $\beta_0 \sim 0.5$, $n_{\rm CSM} \sim 1\ {\rm cm}^{-3}$, $\epsilon_B = \epsilon_e \sim 0.1$) (Nakar & Piran 2011; Sarin et al. 2022), $\nu_{\rm ssa}$ and ν_m are both below 1 GHz, and thus the light curve in all bands above 1 GHz will peak at the deceleration time-scale, which is ~ 3 yr for the KN and ~ 80 yr for the SN.

3 MODELLING

3.1 Fiducial light curves

Here, we show the fiducial non-thermal light curves of SNe/LGRBs and KN/SGRBs at 1 GHz, 100 GHz, 1 keV, and 100 keV. The models are generated with `Redback` (Sarin et al. 2024) using the `tophat_redback` (Lamb, Mandel & Resmi 2018), `PWN` (This work, Appendix A), and `kilonova_afterglow_redback` (Margalit & Piran 2020; Sarin et al. 2022) models for the GRB afterglow, PWN, and ejecta afterglow, respectively. These models for a distance of 100 Mpc are shown in Fig. 1.

The GRB afterglow model is calculated using a jet opening angle of $\theta_{\rm jet} = 0.1$ radians, spectral index $p = 2.5$, initial Lorentz factor $\gamma_0 = 100$, $\epsilon_e = 0.1$, $\epsilon_B = 0.01$, and a jet energy of $E_{\rm jet} = 10^{52}$ erg for the LGRB and 10^{50} erg for the SGRB, which are typical parameters inferred from LGRB and SGRB afterglows (Fong et al. 2015; Wang et al. 2015; Atteia et al. 2017). The models are calculated with two values of $n_{\rm CSM}$: 1 ${\rm cm}^{-3}$ and 10^{-3} ${\rm cm}^{-3}$, representing the high and low ends of typical observed GRBs (Fong et al. 2015; Wang et al. 2015). The models are also calculated with two viewing angles, 0° and 32°, which are referred to as on- and off-axis, respectively. The off-axis angle was chosen as 32° because it is the peak of the inclination distribution for gravitational wave detected sources, and therefore the most likely viewing angle for GW counterparts (Schutz 2011; Lamb & Kobayashi 2017).

The PWN model is calculated using a magnetar braking index[2] $n = 3$, $\epsilon_B = 10^{-2}$, and electron injection Lorentz factor $\gamma_b = 10^{-5}$, which are typical of Galactic PWNe such as the Crab (Tanaka et al. 2020, Tanaka & Takahara 2013) and similar to that used in previous studies of SLSN radio emission (e.g. Omand et al. 2018; Law et al. 2019; Eftekhari et al. 2021). The SN scenario is calculated with initial spin-down luminosity $L_0 = 10^{48}$ erg ${\rm s}^{-1}$, spin-down time-scale $t_{\rm SD} = 10^4$ s, and ejecta mass $M_{\rm ej} = 5M_\odot$ while the KN scenario is calculated with $L_0 = 10^{50}$ erg ${\rm s}^{-1}$, $t_{\rm SD} = 10^2$ s, and $M_{\rm ej} = 0.05M_\odot$. The parameters chosen for the SN scenario give parameters consistent with previous GRB-SN observations and models of SNe Ic-BL (Taddia et al. 2019; Suzuki & Maeda 2021; Omand & Sarin 2024; Srinivasaragavan et al. 2024), while the parameters chosen for the KN scenario are motivated by previous modelling efforts and numerical simulations (e.g. Yu et al. 2013; Siegel & Metzger 2017; Murase et al. 2018; Margalit & Metzger 2019). The KN is also calculated with a different ejecta composition which is broadly consistent which r-process nucleosynthesis and KN spectral simulations (Foucart et al. 2016; Roberts et al. 2017; Vlasov et al. 2017; Hotokezaka et al. 2021; Pognan et al. 2023, 2025), with $Y_{\rm e} \sim 0.4$, $\bar{Z} \sim 40$, and $Y_{\rm fe} \sim 0.02$.

The parameters for the ejecta afterglow are mostly shared with the other models, since $n_{\rm CSM}$ is already set in the GRB afterglow model, $M_{\rm ej}$ is set by the PWN model, and $E_{\rm ej}$ is calculated in the PWN model, and set by L_0, $t_{\rm SD}$, and $M_{\rm ej}$ [see Sarin et al. (2022) and Omand & Sarin (2024) for further details]. The partition parameters are set as $\epsilon_e = \epsilon_B = 0.1$, and the spectral index is taken as $p = 2.5$ (Frail, Waxman & Kulkarni 2000; Frail et al. 2005).

In radio bands, the PWN is always detectable for the fiducial magnetar-driven SN. The viewing angle of the GRB does not impact the time-scale of the detectability of the PWN due to the large difference in peak time-scales. The PWN peak time-scales of the model are $\sim$ a few hundred d at 100 GHz and $\sim$ a decade at 1 GHz, in agreement with what we derived in Section 2. The detectability window of the PWN depends on the ambient density, since both afterglow components decrease in luminosity in more rarefied environments, especially the ejecta afterglow. The GRB afterglow is always the dominant component at early times, and ejecta afterglow at late times. The PWN is the dominant component after $\sim$ 6 yr at 1 GHz and after $\sim$1 yr at 100 GHz, and it is the dominant component in both bands until $\sim$30 yr in the high density medium and until >300 yr in the low-density medium.

The radio emission from the PWN in the fiducial magnetar-driven KN will be detectable in most situations, although in dense environments, the ejecta afterglow will have comparable luminosity at 1 GHz to the PWN at the PWN peak time-scale. The GRB afterglow is the dominant component at early times if the GRB is on-axis or in a dense ambient medium, but will be subdominant to the PWN in a diffuse medium for an off-axis observer. The peak time-scale is set by SSA at 1 GHz and FFA at 100 GHz. The detectability window at 1 GHz in a high-density medium is $\sim$40–150 d, and for a low-density medium the window is $\sim$30–1500 d, while at 100 GHz the window for a high-density medium is 5–90 d and for a low density medium is 5–1500 d.

In X-rays, there are some regions of the parameter space where the PWN does not dominate the light curve on any time-scale in a magnetar-driven SN, due to the similar peak time-scale to the ejecta afterglow. This is the case at 1 keV in a dense medium, and even in a low-density medium, the PWN will not be the dominant component until several decades post-explosion. At 100 keV, the PWN will be the dominant component from $\sim$ 50 d until > 30 yr, and will be preceded by the GRB in each case except for an off-axis afterglow in a high-density medium, which rises on the same time-scale as the PWN but at a lower luminosity.

[2]The braking index n parametrizes the time dependence of the magnetar spin-down (see equation A1). The value $n = 3$ corresponds to vacuum dipole spin down.

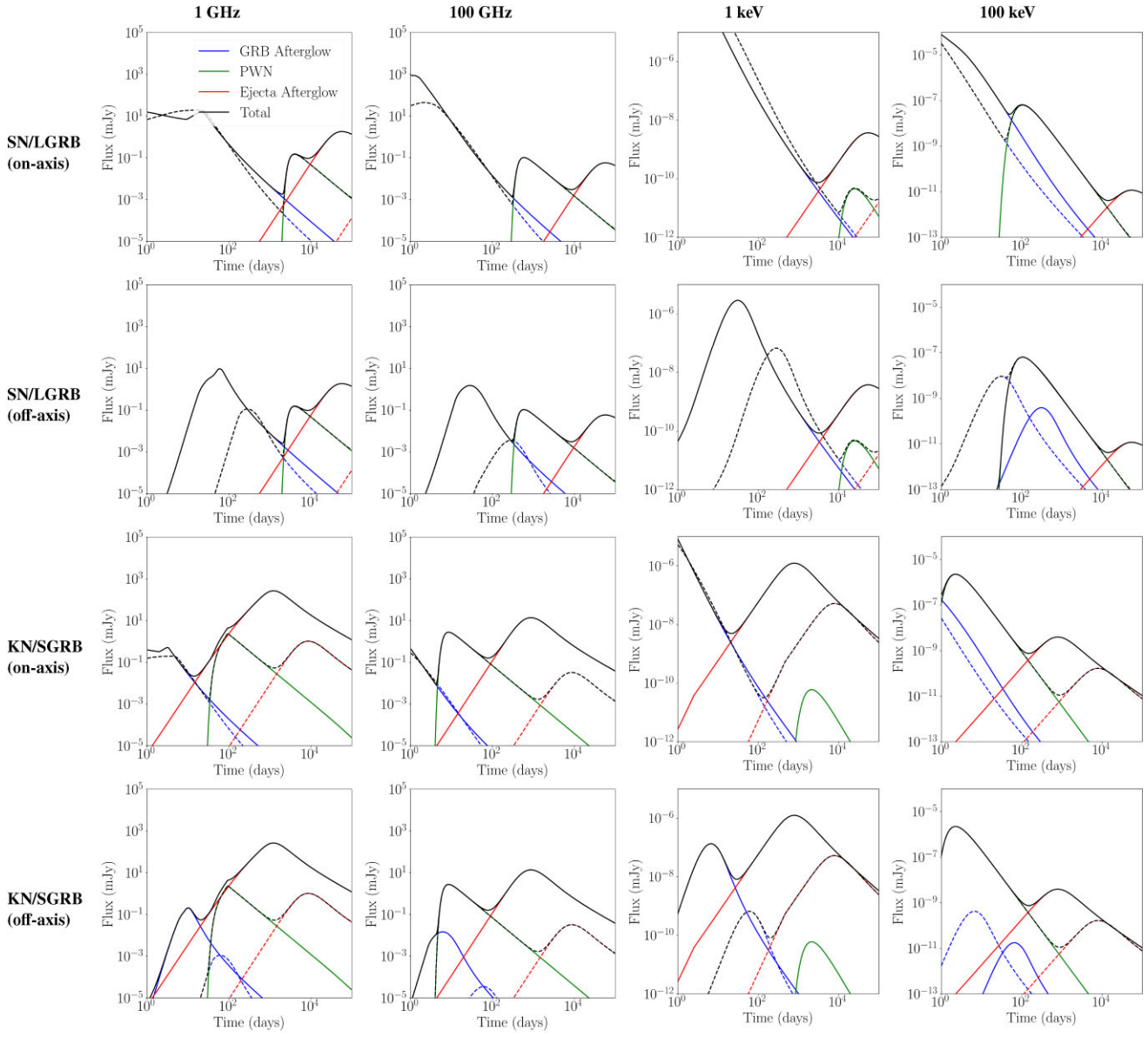

Figure 1. Non-thermal light curves for our fiducial magnetar-driven SNe and KNe, with on- and off-axis GRBs, in radio and X-ray. Each panel shows the GRB afterglow (blue), PWN (green), ejecta afterglow (red), and total emission (black). The solid and dashed lines indicate the density of the ambient medium $n_{\rm CSM}$ to be 1 and 10^{-3} cm^{-3}, respectively. The off-axis afterglow is taken from an observer angle of 32°. The transient is assumed to be at 100 Mpc ($z = 0.024$).

At 1 keV, the PWN in the fiducial magnetar-driven KN will never dominate over the KN afterglow. At 100 keV it dominates from <1 d until ∼ 150 d in a high-density medium and ∼800 d in a low-density medium.

3.2 Inference on a simulated light curve

To determine whether a PWN can be distinguished from an afterglow in data, we simulate and fit an observed radio light curve generated for the fiducial KN/SGRB using the REDBACK simulation workflow at 1 and 100 GHz for up to 100 d post-explosion. The light curves are observed ten times over the time span at each frequency. The distance to the transient is 100 Mpc, giving a redshift of $z = 0.024$; the neutron star merger that causes this transient would thus also be detectable with current gravitational wave detectors (Abbott et al. 2020).

Inference is performed using REDBACK (Sarin et al. 2024) with the PYMULTINEST sampler (Buchner et al. 2014) implemented in BILBY (Ashton et al. 2019). We sample in flux density with a Gaussian likelihood. To gauge whether the PWN is needed to explain the observed emission, we implement a Slab-Spike prior (Malsiner-Walli & Wagner 2018) on the initial PWN luminosity L_0, which imposes a dirac-delta function onto an already existing prior. We give the spike 10 per cent of the probability of the prior and place it at the lowest value of L_0 within the prior. Having a large probability of a low value of L_0 allows us to test if the emission can be reproduced with the PWN effectively turned off. A list of the parameters varied in the inference, as well as the median and 1σ values of the posterior, is found in Table 2. Other parameter values are kept constant at their fiducial values (see Section 3.1).

The fitted data are shown in Fig. 2 and the posterior is shown in Fig. B1. The posteriors for the afterglow parameters $E_{\rm jet}$, $\epsilon_{\rm e,GRB}$,

Table 2. The parameters and priors used in this study. Priors are either uniform (U) log-uniform (L), sine (Sine), or Slab-Spike (S). The values shown for the posterior are the median and 1σ uncertainties. Posterior values denoted with L are given in log-space. The full posterior is shown in Fig. B1.

Parameter	Definition	Units	Injected value	Prior	1D posterior values
$\theta_{\rm v}$	Viewing angle	Radians	0.1	Sine[0,$\pi/2$]	$0.34^{+0.10}_{-0.14}$
$E_{\rm jet}$	Jet energy (isotropic equivalent)	erg	10^{50}	L [10^{46}, 10^{53}]	$L(49.87^{+0.65}_{-0.55})$
$\epsilon_{\rm e,GRB}$	Lepton energy parameter (GRB)		0.1	L [10^{-5}, 1]	$L(-1.07^{+0.44}_{-1.30})$
$\epsilon_{\rm B,GRB}$	Magnetization parameter (GRB)		0.01	L [10^{-5}, 1]	$L(-1.38^{+0.95}_{-1.68})$
$n_{\rm CSM}$	CSM number density	cm^{-3}	10^{-2}	L [10^{-5}, 10^{2}]	$L(0.74^{+0.75}_{-1.15})$
L_0	Initial magnetar spin-down luminosity	erg s^{-1}	10^{50}	S [10^{40}, L[10^{40}, 10^{51}]]	$L(45.46^{+1.15}_{-1.01})$
$t_{\rm SD}$	Spin-down time	s	10^{2}	L [10, 10^{8}]	$L(4.35^{+0.69}_{-0.90})$
$M_{\rm ej}$	Ejecta mass	M$_\odot$	0.05	L [0.01, 100]	$0.02^{+0.00}_{-0.00}$
n	Magnetar braking index		3	U [1.5, 10]	$2.80^{+0.26}_{-0.25}$
$\epsilon_{\rm B,PWN}$	Magnetization parameter (PWN)		10^{-2}	L [10^{-7}, 1]	$L(-1.29^{+0.60}_{-0.56})$
γ_b	Electron injection Lorentz factor		10^{5}	L [10^{2}, 10^{8}]	$L(4.77^{+1.73}_{-1.55})$
$\epsilon_{\rm e,ejecta}$	Lepton energy parameter (ejecta)		0.1	L [10^{-5}, 1]	$L(-3.41^{+1.47}_{-1.05})$
$\epsilon_{\rm B,ejecta}$	Magnetization parameter (ejecta)		0.1	L [10^{-5}, 1]	$L(-3.21^{+1.67}_{-1.18})$

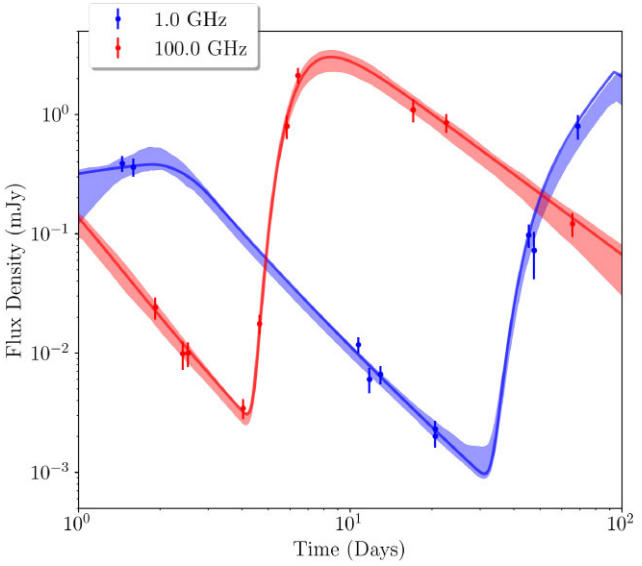

Figure 2. The fitted radio light curve for the simulated KN/SGRB for both 1 and 100 GHz. The solid line shows the model with the highest likelihood while the shaded region shows the 90 per cent confidence interval.

$\epsilon_{\rm B,GRB}$ and as well as n, $\epsilon_{\rm B,PWN}$, and γ_b, are all found to be within around 1σ of the injected parameters. $\theta_{\rm obs}$ and $n_{\rm CSM}$ are more than 1σ away, but are correlated, while $\epsilon_{\rm e,ejecta}$ and $\epsilon_{\rm B,ejecta}$ are not well constrained due to the signal lacking an ejecta afterglow component. The one-dimensional posteriors for L_0 and $t_{\rm SD}$ underestimate and overestimate the injected values, respectively, although the degeneracy between them is clear in the two-dimensional posterior. The ejecta mass is also significantly underestimated. These three parameters all show strong correlation and have wide priors with the injected value close to the edge of the prior. The escape time (equation 6) shows a dependence on both ejecta mass and velocity, so the lower inferred ejecta mass implies that the ejecta in the inferred model must have lower velocity than in the injected model, which is consistent with a lower L_0 and higher $t_{\rm SD}$. This example shows the sensitivity of the inferred parameters to the intrinsic noise of the measurement. Other estimates of $M_{\rm ej}$ or $v_{\rm ej}$ in a real system, either from gravitational wave data (Abbott et al. 2019), KN light curve modelling (Yu et al. 2013; Metzger 2019; Sarin et al. 2022), or KN spectroscopy (Hotokezaka et al. 2021; Pognan et al. 2023), would help get a more accurate estimate of the PWN and ejecta parameters.

The posterior for L_0 shows no probability at 10^{40} erg, showing that it is unlikely that this emission can be reproduced without a strong PWN. The main features that cannot be reproduced by an ejecta afterglow are the frequency-dependent peak time-scales and the fast rise from only GRB afterglow emission to PWN peak. The ejecta afterglow emission time-scale can be frequency-dependent if either the self-absorption frequency or synchrotron frequency of the minimum Lorentz factor is higher than the observed frequency, which can happen at low frequencies in atypical cases. This would cause a dependence of either $t_{\rm peak} \propto \nu_{\rm obs}^{-1/3}$ if ν_m is higher or $t_{\rm peak} \propto \nu_{\rm obs}^{-(4+p)/(3p-2)}$ if $\nu_{\rm ssa}$ is higher (Nakar & Piran 2011), which could mimic the $t_{\rm peak} \propto \nu_{\rm obs}^{-0.42}$ expected for a PWN. However, the rising flux for an ejecta afterglow is a power law that becomes slower ($F_\nu \propto t^{1.5}$ as opposed to $F_\nu \propto t^3$) under the conditions where $t_{\rm peak}$ becomes frequency-dependent (Nakar & Piran 2011). The ejecta afterglow rising flux also contrasts with the PWN rising flux, which is an exponential rise due to being caused by optical depth effects. While this can be used to distinguish between the two scenarios, one needs multiple extremely high cadence observations during the light curve rise to distinguish them via the rise index alone. Another method of confirming the presence of a PWN is to continue observing on $\sim$ year time-scales when the ejecta afterglow component dominates, as the presence of the third peak would provide further evidence for this scenario. However, this is only viable for SGRBs, as the ejecta afterglow is not expected to dominate the emission for LGRBs until decades after the burst.

4 DISCUSSION

Although the PWN can be the dominant emission component at certain times and frequencies, these PWNe are still not bright enough to be seen at large redshifts. The detection limit for NuSTAR in hard X-rays is roughly 1 nJy (Vurm & Metzger 2021), which gives a detection horizon of only $\sim$ 30 Mpc for our fiducial SN/LGRB PWNe and 3 Mpc for our fiducial KN/SGRB PWNe. The Karl G. Jansky Very Large Array (VLA) and Atacama Large Millimetre/submillimetre Array (ALMA) have 3σ detection limits of

roughly 15 and 50 μJy for 1 and 100 GHz, respectively (Omand et al. 2018; Eftekhari et al. 2021). Based on Fig. 1, the detection horizon for our fiducial SN/LGRB PWNe is ~ 250 Mpc ($z \sim 0.06$) at 1 GHz and 200 Mpc ($z \sim 0.05$) at 100 GHz, while for our fiducial KN/SGRB PWN the detection horizon is ~ 1.5 Gpc ($z \sim 0.3$) at 1 GHz and 1.0 Gpc ($z \sim 0.2$) at 100 GHz. The horizon for SNe/LGRBs is lower than almost all Ic-BL SNe (Taddia et al. 2019; Srinivasaragavan et al. 2024) and LGRBs (Horvath et al. 2022); however, the horizon for KNe/SGRBs contains roughly 10 per cent of the SGRB distribution (Ghirlanda et al. 2016). Schroeder et al. (2020) observed several $z < 0.5$ SGRBs at 6 GHz around 2–14 yr post-burst and did not detect any emission, placing constraints on both the PWN and ejecta afterglow emission.

Next-generation radio telescopes, such as DSA-2000 and ngVLA will have 3σ detection limits of ~ 1 μJy in the 1–100 GHz bands (Di Francesco et al. 2019; Hallinan et al. 2019; McKinnon et al. 2019), giving horizons of $\sim$ 1–1.5 Gpc ($z \sim 0.2 - 0.3$) for our fiducial SN/LGRB PWNe and $\sim$ 4–10 Gpc ($z \sim 0.7 - 1.5$) for our fiducial KN/SGRB PWNe. Most classified Ic-BL SNe are detected below the SNe/LGRB horizon (Taddia et al. 2019; Srinivasaragavan et al. 2024), although the majority of LGRBs are at higher redshifts (Lan et al. 2021). The horizon for SGRBs comprises around 50 per cent of the population at 1 GHz and almost the entire population at 100 GHz (Ghirlanda et al. 2016).

We precluded modelling of the optical/UV signal in Section 3.1 due to possible contamination from the associated SN/KN. The thermal SN/KN component can be modelled along with the non-thermal components [see e.g. Wallace & Sarin (2024) for joint afterglow/KN modelling], but we did not want to present four-component models for simplicity. The absorption processes for optical/UV emission are primarily bound-bound transitions that thermalize the energy in the ejecta, and the escape time-scale is thus given by the nebular time-scale for the ejecta. For typical GRB-SNe, this time-scale is around 1–2 months, while for magnetar-driven KNe, this time-scale is around 1–5 d. Models of these transients predict strong optical emission at these times (Sarin et al. 2022; Omand & Sarin 2024), although near-UV emission can decline sharply as the transient cools, leaving a window for the non-thermal emission to be detectable at these wavelengths.

Given the need for well-timed, high-cadence, multiband observations to confirm this scenario, it's important to note the early signals of magnetar-driven GRBs. This is especially important to coordinate facilities like ALMA, which can take as long as two weeks to respond to a target-of-opportunity trigger,[3] which is comparable to the escape time-scale at 100 GHz in the fiducial KN/SGRB. With the horizons calculated above, it is unlikely we will detect PWN emission for all but the closest LGRBs or for SGRBs above $z \approx 0.3$ with current instruments, so it is best to focus on low-redshift SGRBs. Given the potential overlap of the PWN and ejecta afterglow components at lower radio frequencies for SGRBs, targeting the afterglows with high frequency radio observations has a higher chance of a clear discovery, which can be followed up with lower frequency radio observations to further characterize the PWN and ejecta afterglow components. Early signals typically associated with the presence of a central magnetar are X-ray plateaus (Rowlinson et al. 2013; Gompertz et al. 2014; Stratta et al. 2018; Sarin, Lasky & Ashton 2020a) and extended emission (Metzger et al. 2008; Bucciantini et al. 2012; Gompertz et al. 2013; Gompertz et al. 2014; Gibson et al. 2017; Sarin, Lasky & Ashton 2020b). For closer objects, a gravitational wave detection of a BNS merger coincident with the GRB showing a low chirp mass and an anomalously bright KN (Yu et al. 2013; Metzger 2019; Sarin et al. 2022; Ai et al. 2025) would mark it as a strong candidate for being magnetar-powered. BNS mergers are also expected to be neutrino sources on a short time-scale (Kyutoku & Kashiyama 2018), but a long-lived magnetar remnant could emit neutrinos on a longer time-scale due to the interaction of the hadrons in the pulsar wind and ejecta (Bednarek 2003; Di Palma, Guetta & Amato 2017).

The presence of a magnetar engine can be inferred from the luminosity and time-scale of the thermal transient or the detection of non-thermal emission from the PWN, but the magnetar may also have other detectable effects. Omand et al. (2019) suggested that dust formed in the ejecta of magnetar-driven SNe can be heated by the PWN and produce an observable signal in the infrared. While this signal could be present in GRB-SNe, those systems could also have an infrared excess due to r-process nucleosynthesis in a collapsar (Siegel, Barnes & Metzger 2019; Barnes & Metzger 2022; Anand et al. 2024), so this signal would not be definitive. In KNe with no energy injection into the ejecta, dust is difficult to form due to the low density of the ejecta (Takami, Nozawa & Ioka 2014); adding energy injection would only make this problem worse due to the slower cooling and faster ejecta velocity, so this is likely not a viable method of detecting magnetars in KNe. Also, KNe are intrinsically bright in the infrared, so an infrared excess from dust would be difficult to disentangle from the KN emission. The PWN can also ionize the ejecta, leading to higher ionization lines in the nebular optical/UV spectrum of the transient. This effect has been examined in stripped-envelope SNe (Chevalier & Fransson 1992; Dessart 2019; Omand & Jerkstrand 2023; Dessart 2024), with recent efforts focused on replicating the spectrum of possible magnetar-driven SN, such as SN 2012au (Milisavljevic et al. 2013, 2018). However, these spectral models are still missing key physics to make accurate predictions for these systems [see Omand & Jerkstrand (2023) for details]. The ejecta velocity of a magnetar-driven KN is expected to be $\gtrsim 0.4c$ (Sarin et al. 2022), so most lines would likely be broadened too much to be detectable. Models of nebular spectra are also extremely uncertain due to a lack of atomic data (Hotokezaka et al. 2023; Pognan et al. 2023; Banerjee et al. 2025; Pognan et al. 2025), so increasing the complexity of those models with a central energy source would likely be unfeasible for the foreseeable future. A PWN could also induce polarization in the ejecta either by injecting energy asymmetrically (Inserra et al. 2016; Saito et al. 2020) or by causing hydrodynamic instabilities in the ejecta (Chen et al. 2016; Suzuki & Maeda 2017, 2021). Modelling of polarization in similar systems is scarce (Tanaka et al. 2017; Bulla et al. 2019) and their polarization without a central magnetar is not well understood, so a polarization measurement will not be able to constrain the presence of a magnetar without further modelling.

Modelling the three different emission components and their interactions is extremely difficult, and our simplified treatment of the non-thermal emission components has a few notable caveats. The PWN and transient ejecta are assumed to be spherical in this model, although in reality this symmetry can be broken in plenty of ways. Most numerical simulations of KNe show large deviations from spherical symmetry (Bauswein, Goriely & Janka 2013; Hotokezaka et al. 2013; Rosswog et al. 2014), and interaction between the jet and ejecta can cause the geometry and emission of both to be affected (Nativi et al. 2021, 2022). The PWN can be aspherical due to Kelvin–Helmholtz instabilities, and the nebula can also cause strong Rayleigh–Taylor instabilities within the transient ejecta, which can form ejecta filaments (Davidson & Fesen 1985;

[3] https://almascience.eso.org/observing/too-activation

Jun 1998; Bucciantini et al. 2004; Porth, Komissarov & Keppens 2014) and cause the PWN forward shock to break out of the material (Blondin & Chevalier 2017; Suzuki & Maeda 2017; Omand et al. 2025). The rebrightenings could also be caused by more complicated jet geometries and afterglow physics, such as an exotic jet shape (Takahashi & Ioka 2021; Beniamini, Gill & Granot 2022), counterjet (Granot & Loeb 2003; Li & Song 2004; Wang, Huang & Kong 2009; Zhang & MacFadyen 2009; Dastidar & Duffell 2024), reverse shock (Kobayashi, Piran & Sari 1999; Kobayashi & Sari 2000; Uhm et al. 2012), or late energy injection into the shock, causing a refreshed shock (Panaitescu, Mészáros & Rees 1998; Rees & Mészáros 1998; Zhang & Mészáros 2002). However, the peak time-scales for reverse shocks and counterjets are expected to be much shorter (Kobayashi & Sari 2000; Uhm et al. 2012) and longer (e.g. van Eerten, van der Horst & MacFadyen 2012), respectively. The GRB and ejecta afterglow models we use both assume the surrounding medium has constant density, which is not true in the case of wind or eruptive mass loss from the progenitor. The top-hat model also ignores the effects of the magnetar on the jet itself, which could produce an X-ray plateau in the early afterglow (Rowlinson et al. 2013; Gompertz et al. 2014; Stratta et al. 2018). The use of a one-zone spherical ejecta afterglow also neglects the effects of the density structure of the ejecta, which can cause over an order of magnitude difference in the observed signal (Rosswog et al. 2024).

Radio and hard X-ray opacities are relatively straightforward to compute, but our treatment of the soft X-ray opacity from photoabsorption (equation A12) neglects a lot of complicated physics). In general, the photoabsorption opacity depends on both the composition and time-dependent ionization state of the ejecta, which depends on the luminosity and spectrum of the ionizing PWN radiation and the recombination rates from the relevant ions. We include some compositional dependence with $\bar{Z}$, but neglect the changes in opacity due to changes in ionization, which require detailed radiative transfer simulations to compute. Kashiyama et al. (2016) uses the same treatment and notes that it likely overestimates the photoabsorption opacity. The PWN can drive an ionization front through the ejecta, which can produce UV/soft X-ray emission if it breaks out; Metzger et al. (2014) and Metzger & Piro (2014) discuss this case for magnetar-driven SLSNe and KNe, respectively, and outline the conditions where it can happen. X-ray surveys of SLSNe have shown soft X-ray emission in some cases (Levan et al. 2013), although this emission is rare overall (Margutti et al. 2018). Nebular spectra of potential magnetar-driven supernovae generally show line emission from species that would be ionized out given a soft X-ray breakout, so this phenomenon must be rare. Examining Fig. 1 shows that a decrease in the soft X-ray opacity may lead the PWN to dominate the emission on 1000 d time-scales for the SN/LGRB case, but it is still unlikely for the PWN to dominate in the KN/SGRB case unless the ambient density is extremely low due to the relative brightness of the ejecta afterglow. However, this emission is not predicted to be detectable by something like Chandra unless the transient is extremely close.

The parameters used for the microphysics of our fiducial PWN are consistent with that of Galactic PWNe such as the Crab (Tanaka et al. 2020, Tanaka & Takahara 2013), the lack of observed radio counterparts (Law et al. 2019; Eftekhari et al. 2021) shows that this assumption may not be correct for most magnetar-driven SNe. A couple of alternate microphysical models are the high-magnetization PWN model (Murase et al. 2021), where the synchrotron energy peaks in the MeV range, and the low-magnetization model (Vurm & Metzger 2021), where the emission is dominated by inverse-Compton emission ($Y_{\rm IC} \gtrsim 10$). The latter of these models

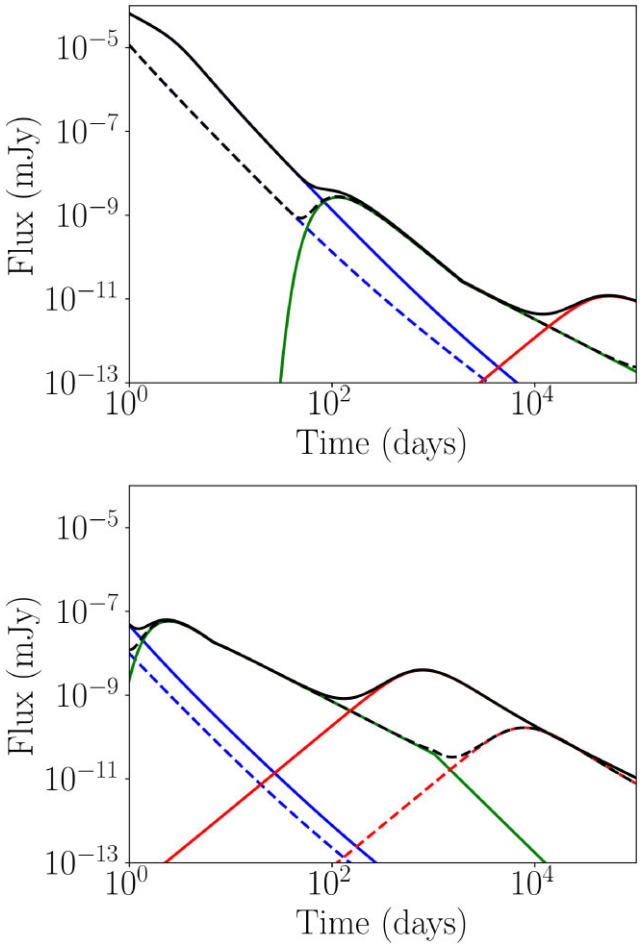

Figure 3. 100 keV light curves for magnetar-driven SNe and KNe with an on-axis GRB and a high-magnetization PWN. Each panel shows the GRB afterglow (blue), PWN (green), ejecta afterglow (red), and total emission (black). The solid and dashed lines indicate the density of the ambient medium $n_{\rm CSM}$ to be 1 and 10^{-3} cm^{-3} respectively.

is also motivated by strong non-thermal losses in SLSNe (Vurm & Metzger 2021). The radio emission from both of these cases would be significantly lower than the Crab-like case (Murase et al. 2021).

Because our model does not include inverse Compton emission for simplicity, we cannot treat the low-magnetization model, but we can examine the high-magnetization model further. Fig. 3 shows the 100 keV light curves for our fiducial SN/LGRB and KN/SGRB with $\epsilon_{\rm B,PWN} = 0.5$, $\gamma_b = 10^7$, and the low-energy spectral index $q_1 = 1$, as used in Murase et al. (2021). The PWN signal at 100 keV for both types of objects is lower than the cases with Crab-like microphysics due to the peak of the spectrum being in the 10–100 MeV range and the steeper spectral index. This is consistent with Vurm & Metzger (2021) and Murase et al. (2021), which show the two models having emission of around the same order of magnitude at 100 keV. Those studies also show that detecting the emission at >1 MeV will likely require next generation instruments, such as eASTROGAM and AMEGO. While it may be possible to have a synchrotron spectrum that peaks at ∼100 keV around the PWN escape time, such a model would likely need to be fine-tuned and require more physical motivation.

The SGRB counterpart to the BNS merger GW170817, GRB170817A, is the closest SGRB to date (Fong et al. 2022; Nugent et al. 2022) and one of the most studied transients in history (e.g.

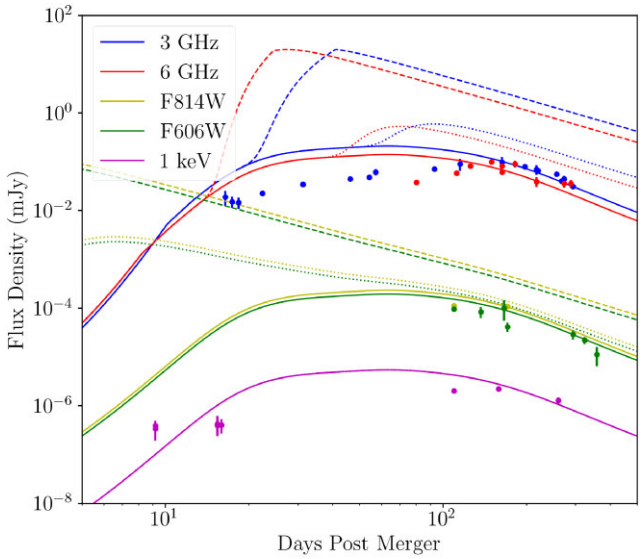

Figure 4. The GRB afterglow of GRB170817A in optical, X-ray, and radio (Evans et al. 2017; Haggard et al. 2017; Hallinan et al. 2017; Mooley et al. 2018) and a Gaussian jet light-curve model using the median parameters from Lamb et al. (2019a). PWNe from magnetars with $L_0 = 10^{50}$ ($E_{\rm rot} = 10^{52}$) and $L_0 = 10^{49}$ ($E_{\rm rot} = 10^{51}$) are shown with dashed and dotted lines, respectively, while the afterglow with no PWN is shown with solid lines. The other PWN parameters are taken from the fiducial KN/SGRB case.

Abbott et al. 2017a, b, c; Margutti & Chornock 2021). The total mass of the BNS system was inferred to be $\sim 2.7\ M_\odot$ (Abbott et al. 2019) with $< 0.1\ M_\odot$ of ejected material, which is larger than the inferred maximum non-rotating neutron star mass $M_{\rm TOV}$ of 2.2–2.3 $M_\odot$. However, several studies propose that GW170817 could have had a long-lived or infinitely stable neutron star, especially if the spin-down luminosity is dominated by gravitational wave emission (Ai et al. 2018; Yu, Liu & Dai 2018; Piro et al. 2019; Sarin & Lasky 2021; DuPont & MacFadyen 2024). Fig. 4 shows the afterglow of GRB170817A in optical, X-ray, and radio (Evans et al. 2017; Haggard et al. 2017; Hallinan et al. 2017; Lyman et al. 2018; Mooley et al. 2018), along with a Gaussian jet light curve model using the median parameters from Lamb et al. (2019a). We note that the afterglow models used here and in Lamb et al. (2019a) have slightly different physics,[4] and thus our model does not match the data exactly. We do not model the emission from a KN component here, and the optical opacity for absorption of PWN emission is taken as $\kappa = 1$ cm ; Metzger & Fernández 2014; Lippuner et al. 2017). We show a GRB afterglow without a PWN and two with initial magnetar luminosities of $L_0 = 10^{50}$ ($E_{\rm rot} = 10^{52}$) and $L_0 = 10^{49}$ ($E_{\rm rot} = 10^{51}$), with all other parameters being taken from the fiducial case. With a PWN, both the optical and radio emission are significantly more luminous than observed, and the radio emission shows a distinctive rise at around 10–100 d, would would have been readily observable. The optical emission would have also risen on the time-scale of 1–2 d and would have been detectable in the initial KN emission. This shows that if the remnant of the 170 817 BNS merger is a stable neutron star, the rotational energy of the neutron star emitted in electromagnetic radiation would have to be $\lesssim 10^{51}$ erg in order to not be detectable in the afterglow, which gives a conservative lower limit on the initial spin period of ~ 7 ms for a 2.2 $M_\odot$ neutron star, similar to what was found by Murase et al. (2018). A remnant neutron star with initial spin period of < 7 ms would also have increased the KN bolometric luminosity by 1–3 orders of magnitude (Sarin et al. 2022) depending on the exact spin period, which would have been detectable for spin periods ~ 1 ms but may not be for spin periods ~ 5 ms due to uncertainties in KN motdelling (Brethauer et al. 2024; Sarin & Rosswog 2024; Pognan et al. 2025).

A recent case is GRB210702A, which showed a frequency-dependent rebrightening as predicted by the PWN model (de Wet et al. 2024). However, GRB210702A is an LGRB at $z = 1.160$ (Xu et al. 2021) with the rebrightening starting at ~ 10 d in the observer frame, bringing the rest frame rebrightening time to ~ 5 d. Given the time-scale from equation (6), this would require $\lesssim 0.01\ M_\odot$ of ejecta traveling at a significant fraction of the speed of light, which is unrealistic for even a KN. The distance is also far outside the expected horizon for our fiducial parameters, so the effect of the PWN would be difficult to observe in this object. Thus, it seems unlikely that the source of the rebrightening could be a PWN.

5 SUMMARY

Non-thermal light curves from magnetar-powered GRBs can show emission from the GRB afterglow, PWN, and ejecta afterglow. The time-scales for the peak of each emission component are different in both radio and x-ray for our fiducial parameters, making each component potentially distinguishable in the resulting light curve. The GRB afterglow will peak first, followed by the PWN, then the ejecta afterglow. The GRB and ejecta afterglow peak time-scales are set by the deceleration time-scale and the movement of the spectral peak across the band, while the PWN peak time-scale is set by absorption processes within the transient ejecta, giving different behaviours across different bands for the peak time-scales.

We show the light curves for fiducial SNe/LGRBs and KNe/SGRBs, both on- and off-axis, at 1 GHz, 100 GHz, 1 keV, and 100 keV. At 1 GHz, the PWN dominates the emission at ~ 6 yr for SNe/LGRBs and ~ 100 d for KN/SGRBs, although PWN can be subdominant to a KN afterglow if the density of the surrounding medium is high enough. At 100 GHz, the PWN dominates the emission at ~ 1 yr for SNe/LGRBs and ~ 15 d for KN/SGRBs, regardless of the density of the ambient medium. The PWN will never be detectable at 1 keV due to strong absorption, and while the PWN does dominate the 100 keV emission over the first few decades, the emission is faint enough that detecting it with current instruments is impossible.

We simulate our fiducial KN/SGRB observed at 1 and 100 GHz and fit it with a three-component model using a prior that can effectively turn off the PWN component. The posterior shows a 0 per cent probability that the transient can be explained without a PWN component. The two distinguishing features of the PWN component are the frequency-dependent rise and the fast rise from only afterglow emission to PWN peak. The ejecta afterglow can show a frequency-dependent rise time in atypical cases, but the rise will slow down in those cases, making it possible to distinguish through high-cadence observations.

The detection horizon for the fiducial PWN in these scenarios is $z \sim 0.05$–0.06 for SN/LGRBs and $z \sim 0.2$–0.3 for KN/SGRBs with current instruments and $z \sim 0.2$–0.3 for SN/LGRBs and $z \sim 0.7$–1.5 for KN/SGRBs with next-generation instruments. The PWN emission would be detectable in optical, but will likely compete with the thermal emission from the transient. Our simple treatment of the

[4]Our model has updated versions of jet spreading and SSA compared to Lamb et al. (2019a). Our use of median parameters instead of the most likely parameters will also cause some discrepancy between our light curve and the data.

emission components neglects asymmetry and interaction between the different components, which can have a strong effect but is difficult to describe in a self-consistent way. We modeled the potential non-thermal emission from GRB170817A and GRB210702A and found that neither of them are likely to contain a PWN. The optimal observing strategy for detecting PWNe in GRB afterglows is multiband, high-cadence radio follow-up from 10 to 100 d of nearby SGRBs with an X-ray plateau or extended emission.

ACKNOWLEDGEMENTS

The authors thank Simon de Wet for sharing the data for GRB210702A, Shiho Kobayashi and Cairns Turnbull for helpful discussions, and the anonymous referee for their helpful comments. CMBO and GPL acknowledge support from the Royal Society (grant nos. DHF-R1-221175 and DHF-ERE-221005). NS acknowledges support from the Knut and Alice Wallenberg Foundation through the 'Gravity Meets Light' project and by the research environment grant 'Gravitational Radiation and Electromagnetic Astrophysical Transients' (GREAT) funded by the Swedish Research Council (VR) under Dnr 2016–06012.

DATA AVAILABILITY

The models are available for public use within REDBACK (Sarin et al. 2024).

REFERENCES

Abbott B. P. et al., 2017a, ApJ, 848, L12
Abbott B. P. et al., 2017b, ApJ, 848, L13
Abbott B. P. et al., 2017c, ApJ, 850, L39
Abbott B. P. et al., 2019, Phys. Rev., 9, 011001
Abbott B. P. et al., 2020, Living Rev. Rel., 23, 3
Ai S., Gao H., Dai Z.-G., Wu X.-F., Li A., Zhang B., Li M.-Z., 2018, ApJ, 860, 57
Ai S., Gao H., Zhang B., 2025, ApJ, 978, 52
Anand S. et al., 2024, ApJ, 962, 68
Arnett W. D., 1982, ApJ, 253, 785
Ashton G. et al., 2019, ApJS, 241, 27
Atteia J. L. et al., 2017, ApJ, 837, 119
Banerjee S., Jerkstrand A., Badnell N. et al., 2025, preprint (arXiv:2501.18345)
Barnes J., Metzger B. D., 2022, ApJ, 939, L29
Bauswein A., Goriely S., Janka H. T., 2013, ApJ, 773, 78
Bednarek W., 2003, A&A, 407, 1
Beniamini P., Gill R., Granot J., 2022, MNRAS, 515, 555
Bietenholz M. F., Kronberg P. P., Hogg D. E., Wilson A. S., 1991, ApJ, 373, L59
Blandford R. D., McKee C. F., 1976, Phys. Fluids, 19, 1130
Blandford R. D., McKee C. F., 1977, MNRAS, 180, 343
Blandford R. D., Payne D. G., 1982, MNRAS, 199, 883
Blandford R. D., Znajek R. L., 1977, MNRAS, 179, 433
Blinnikov S. I., Novikov I. D., Perevodchikova T. V., Polnarev A. G., 1984, Sov. Astron. Lett., 10, 177
Blondin J. M., Chevalier R. A., 2017, ApJ, 845, 139
Bochenek C. D., Dwarkadas V. V., Silverman J. M., Fox O. D., Chevalier R. A., Smith N., Filippenko A. V., 2018, MNRAS, 473, 336
Bostancı Z. F., Kaneko Y., Göğüş E., 2013, MNRAS, 428, 1623
Brethauer D. et al., 2024, ApJ, 975, 213
Bucciantini N., Amato E., Bandiera R., Blondin J. M., Del Zanna L., 2004, A&A, 423, 253
Bucciantini N., Metzger B. D., Thompson T. A., Quataert E., 2012, MNRAS, 419, 1537
Buchner J. et al., 2014, A&A, 564, A125
Bugli M., Guilet J., Obergaulinger M., 2021, MNRAS, 507, 443
Bulla M. et al., 2019, Nat. Astron., 3, 99
Cano Z., Wang S.-Q., Dai Z.-G., Wu X.-F., 2017, Adv. Astron., 2017, 8929054
Chen K.-J., Woosley S. E., Sukhbold T., 2016, ApJ, 832, 73
Chen T. W., Brennan S. J., Wesson R. et al., 2021, preprint (arXiv:2109.07942)
Chevalier R. A., Fransson C., 1992, ApJ, 395, 540
Chevalier R. A., Fransson C., 1994, ApJ, 420, 268
Clark D. H. et al., 1983, MNRAS, 204, 415
Corsi A. et al., 2023, ApJ, 953, 179
Dainotti M. G., Nagataki S., Maeda K., Postnikov S., Pian E., 2017, A&A, 600, A98
Dastidar R. G., Duffell P. C., 2024, ApJ, 976, 252
Davidson K., Fesen R. A., 1985, ARA&A, 23, 119
Dessart L., 2019, A&A, 621, A141
Dessart L., 2024, A&A, 692, A204
de Wet S., Laskar T., Groot P. J. et al., 2024, ApJ, 974, 279
Di Francesco J. et al., 2019, in Canadian Long Range Plan for Astronomy and Astrophysics White Papers, 32, preprint (arXiv:1911.01517)
Di Palma I., Guetta D., Amato E., 2017, ApJ, 836, 159
Drout M. R. et al., 2016, ApJ, 821, 57
DuPont M., MacFadyen A., 2024, ApJ, 971, L24
Duncan R. C., Thompson C., 1992, ApJ, 392, L9
Dwarkadas V. V., 2014, MNRAS, 440, 1917
van Dyk S. D., Weiler K. W., Sramek R. A., Rupen M.P., Panagia N., 1994, ApJ, 432, L115
van Eerten H., van der Horst A., MacFadyen A., 2012, ApJ, 749, 44
Eftekhari T. et al., 2019, ApJ, 876, L10
Eftekhari T. et al., 2021, ApJ, 912, 21
Eichler D., Livio M., Piran T., Schramm D. N., 1989, Nature, 340, 126
Evans P. A. et al., 2017, Science, 358, 1565
Fong W. et al., 2015, ApJ, 815, 102
Fong W. et al., 2021, ApJ, 906, 127
Fong W.-f. et al., 2022, ApJ, 940, 56
Foucart F. et al., 2016, Phys. Rev. D, 93, 044019
Frail D. A., Waxman E., Kulkarni S. R., 2000, ApJ, 537, 191
Frail D. A., Soderberg A. M., Kulkarni S. R., Berger E., Yost S., Fox D. W., Harrison F. A., 2005, ApJ, 619, 994
Fransson C. et al., 2014, ApJ, 797, 118
Gaensler B. M., Manchester R. N., Staveley-Smith L., Tzioumis A. K., Reynolds J. E., Kesteven M. J., 1997, ApJ, 479, 845
Gehrels N., Mészáros P., 2012, Science, 337, 932
Gendre B. et al., 2013, ApJ, 766, 30
Ghirlanda G. et al., 2016, A&A, 594, A84
Gibson S. L., Wynn G. A., Gompertz B. P., O'Brien P. T., 2017, MNRAS, 470, 4925
Gkini A. et al., 2024, A&A, 685, A20
Gomez S. et al., 2024, MNRAS, 535, 471
Gompertz B. P. O'Brien P. T. Wynn G. A. Rowlinson A. 2013, MNRAS, 431, 1745
Gompertz B. P., O'Brien P. T., Wynn G. A., 2014, MNRAS, 438, 240
Granot J., Loeb A., 2003, ApJ, 593, L81
Granot J., Panaitescu A., Kumar P., Woosley S. E., 2002, ApJ, 570, L61
Greiner J. et al., 2015, Nature, 523, 189
Haggard D., Nynka M., Ruan J. J., Kalogera V., Cenko S. B., Evans P., Kennea J. A., 2017, ApJ, 848, L25
Hajela A. et al., 2022, ApJ, 927, L17
Hallinan G. et al., 2017, Science, 358, 1579
Hallinan G., et al., 2019, in Bulletin of the American Astronomical Society, 255, preprint (arXiv:1907.07648)
Horvath I., Racz I. I., Bagoly Z. et al., 2022, Universe, 8, 221
Hotokezaka K., Kiuchi K., Kyutoku K., Okawa H., Sekiguchi Y.-I., Shibata M., Taniguchi K., 2013, Phys. Rev. D, 87, 024001
Hotokezaka K., Nissanke S., Hallinan G., Lazio T. J. W., Nakar E., Piran T., 2016, ApJ, 831, 190
Hotokezaka K., Tanaka M., Kato D., Gaigalas G., 2021, MNRAS, 506, 5863
Hotokezaka K., Tanaka M., Kato D., Gaigalas G., 2023, MNRAS, 526, L155
Illarionov A. F., Sunyaev R. A., 1975, A&A, 39, 185
Inserra C., Bulla M., Sim S. A., Smartt S. J., 2016, ApJ, 831, 79

Ioka K., Nakamura T., 2018, Prog. Theor. Exp. Phys., 2018, 043E02
Jerkstrand A. et al., 2017, ApJ, 835, 13
Jin Z.-P. et al., 2016, Nat. Commun., 7, 12898
Jin Z.-P., Covino S., Liao N.-H., Li X., D'Avanzo P., Fan Y.-Z., Wei D.-M., 2020, Nat. Astron., 4, 77
Jun B.-I., 1998, ApJ, 499, 282
Kaneko Y., Bostancı Z. F., Göğüş E., Lin L., 2015, MNRAS, 452, 824
Kangas T. et al., 2022, MNRAS, 516, 1193
Kashiyama K., Murase K., Bartos I., Kiuchi K., Margutti R., 2016, ApJ, 818, 94
Kennel C. F., Coroniti F. V., 1984, ApJ, 283, 694
Klein O., Nishina T., 1929, Zeitschrift fur Physik, 52, 853
Kobayashi S., Sari R., 2000, ApJ, 542, 819
Kobayashi S., Piran T., Sari R., 1999, ApJ, 513, 669
Kool E. C. et al., 2023, Nature, 617, 477
Kouveliotou C. et al., 1993, ApJ, 413, L101
Kusafuka Y., Matsuoka T., Sawada R., 2025, preprint (arXiv:2503.13291)
Kyutoku K., Kashiyama K., 2018, Phys. Rev. D, 97, 103001
Lamb G. P., Kobayashi S., 2017, MNRAS, 472, 4953
Lamb G. P., Mandel I., Resmi L., 2018, MNRAS, 481, 2581
Lamb G. P. et al., 2019a, ApJ, 870, L15
Lamb G. P. et al., 2019b, ApJ, 883, 48
Lan G.-X., Wei J.-J., Zeng H.-D., Li Y., Wu X.-F., 2021, MNRAS, 508, 52
Lang K. R., 1999, Astrophysical Formulae. Springer, New York
Lasky P. D., Leris C., Rowlinson A., Glampedakis K., 2017, ApJ, 843, L1
Lattimer J. M., Schramm D. N., 1976, ApJ, 210, 549
Law C. J. et al., 2019, ApJ, 886, 24
Levan A. J., Read A. M., Metzger B. D., Wheatley P. J., Tanvir N. R., 2013, ApJ, 771, 136
Levan A. J. et al., 2014, ApJ, 781, 13
Levan A. J. et al., 2024, Nature, 626, 737
Li Z., Song L. M., 2004, ApJ, 614, L17
Lippuner J. et al., 2017, MNRAS, 472, 904
Lovelace R. V. E., Romanova M. M., Bisnovatyi-Kogan G. S., 1999, ApJ, 514, 368
Lyman J. D. et al., 2018, Nat. Astron., 2, 751
MAGIC Collaboration, 2019, Nature, 575, 459
MacFadyen A. I., Woosley S. E., 1999, ApJ, 524, 262
MacFadyen A. I., Woosley S. E., Heger A., 2001, ApJ, 550, 410
Maeda K., Nakamura T., Nomoto K., Mazzali P. A., Patat F., Hachisu I., 2002, ApJ, 565, 405
Malsiner-Walli G., Wagner H., 2018, preprint (arXiv:1812.07259)
Margalit B., Metzger B. D., 2019, ApJ, 880, L15
Margalit B., Piran T., 2020, MNRAS, 495, 4981
Margalit B. et al., 2018, MNRAS, 481, 2407
Margutti R., Chornock R., 2021, ARA&A, 59, 155
Margutti R. et al., 2018, ApJ, 864, 45
Margutti R. et al., 2023, ApJ, 954, L45
Mazzali P. A., McFadyen A. I., Woosley S. E., Pian E., Tanaka M., 2014, MNRAS, 443, 67
McKinnon M., Beasley A., Murphy E. et al., 2019, in Bulletin of the American Astronomical Society 81
Mészáros P., 2006, Rep. Prog. Phys., 69, 2259
Metzger B. D., 2019, Living Rev. Rel., 23, 1
Metzger B. D., Fernández R., 2014, MNRAS, 441, 3444
Metzger B. D., Piro A. L., 2014, MNRAS, 439, 3916
Metzger B. D., Quataert E., Thompson T. A., 2008, MNRAS, 385, 1455
Metzger B. D., Vurm I., Hascoët R., Beloborodov A.M., 2014, MNRAS, 437, 703
Milisavljevic D. et al., 2013, ApJ, 770, L38
Milisavljevic D. et al., 2018, ApJ, 864, L36
Mondal S., Bera A., Chandra P., Das B., 2020, MNRAS, 498, 3863
Mooley K. P. et al., 2018, Nature, 554, 207
Mösta P. et al., 2020, ApJ, 901, L37
Murase K., Kashiyama K., Kiuchi K., Bartos I., 2015, ApJ, 805, 82
Murase K., Kashiyama K., Mészáros P., 2017, MNRAS, 467, 3542
Murase K. et al., 2018, ApJ, 854, 60
Murase K. et al., 2021, MNRAS, 508, 44
Nakar E., Piran T., 2011, Nature, 478, 82
Nakar E., Piran T., Granot J., 2002, ApJ, 579, 699
Nakauchi D., Kashiyama K., Suwa Y. et al., 2013, ApJ, 778, 67
Nativi L. et al., 2021, MNRAS, 500, 1772
Nativi L. et al., 2022, MNRAS, 509, 903
Nicholl M., Guillochon J., Berger E., 2017, ApJ, 850, 55
Norris J. P., Bonnell J. T., 2006, ApJ, 643, 266
Nousek J. A. et al., 2006, ApJ, 642, 389
Nugent A. E. et al., 2022, ApJ, 940, 57
O'Brien P. T. et al., 2006, ApJ, 647, 1213
Omand C. M. B., Jerkstrand A., 2023, A&A, 673, A107
Omand C. M. B., Sarin N., 2024, MNRAS, 527, 6455
Omand C. M. B., Kashiyama K., Murase K., 2018, MNRAS, 474, 573
Omand C. M. B., Kashiyama K., Murase K., 2019, MNRAS, 484, 5468
Omand C. M. B., Sarin N., Temim T., 2025, MNRAS, 536, 408
Paczynski B., Rhoads J. E., 1993, ApJ, 418, L5
Panaitescu A., Mészáros P., Rees M. J., 1998, ApJ, 503, 314
Piran T., 2004, Rev. Mod. Phys., 76, 1143
Piro L. et al., 2019, MNRAS, 483, 1912
Pognan Q. et al., 2023, MNRAS, 526, 5220
Pognan Q., Wu M.-R., Martínez-Pinedo G., da Silva R. F., Jerkstrand A., Grumer J., Flörs A., 2025, MNRAS, 536, 2973
Poidevin F. et al., 2022, MNRAS, 511, 5948
Poidevin F. et al., 2023, MNRAS, 521, 5418
Popham R., Woosley S. E., Fryer C., 1999, ApJ, 518, 356
Porth O., Komissarov S. S., Keppens R., 2014, MNRAS, 443, 547
Pursiainen M. et al., 2022, A&A, 666, A30
Pursiainen M. et al., 2023, A&A, 674, A81
Rastinejad J. C. et al., 2022, Nature, 612, 223
Rees M. J., Meszaros P., 1992, MNRAS, 258, 41
Rees M. J., Mészáros P., 1998, ApJ, 496, L1
Roberts L. F. et al., 2017, MNRAS, 464, 3907
Romanova M. M., Ustyugova G. V., Koldoba A. V., Lovelace R. V. E., 2005, ApJ, 635, L165
Rossi E., Lazzati D., Rees M. J., 2002, MNRAS, 332, 945
Rosswog S., Korobkin O., Arcones A., Thielemann F.-K., Piran T., 2014, MNRAS, 439, 744
Rosswog S., Diener P., Torsello F., Tauris T. M., Sarin N., 2024, MNRAS, 530, 2336
Rowlinson A., O'Brien P. T., Metzger B. D., Tanvir N. R. , Levan A. J., 2013, MNRAS, 430, 1061
Saito S. et al., 2020, ApJ, 894, 154
Sari R., Piran T., 1995, ApJ, 455, L143
Sari R., Piran T., Narayan R., 1998, ApJ, 497, L17
Sarin N., Lasky P. D., 2021, Gen. Relativ. Gravit., 53, 59
Sarin N., Rosswog S., 2024, ApJ, 973, L24
Sarin N., Lasky P. D., Ashton G., 2019, ApJ, 872, 114
Sarin N., Lasky P. D., Ashton G., 2020a, Phys. Rev. D, 101, 063021
Sarin N., Lasky P. D., Ashton G., 2020b, MNRAS, 499, 5986
Sarin N. et al., 2022, MNRAS, 516, 4949
Sarin N. et al., 2024, MNRAS, 531, 1203
Schroeder G. et al., 2020, ApJ, 902, 82
Schutz B. F., 2011, Class. Quantum Gravity, 28, 125023
Siegel D. M., Metzger B. D., 2017, Phys. Rev. Lett., 119, 231102
Siegel D. M., Barnes J., Metzger B. D., 2019, Nature, 569, 241
Smith N., Chornock R., Li W., Ganeshalingam M., Silverman J. M., Foley R. J., Filippenko A. V., Barth A. J., 2008, ApJ, 686, 467
Srinivasaragavan G. P. et al., 2024, ApJ, 976, 71
Stratta G., Dainotti M. G., Dall'Osso S., Hernandez X., De Cesare G., 2018, ApJ, 869, 155
Sun L., Xiao L., Li G., 2022, MNRAS, 513, 4057
Suzuki A., Maeda K., 2017, MNRAS, 466, 2633
Suzuki A., Maeda K., 2021, ApJ, 908, 217
Taddia F. et al., 2019, A&A, 621, A71
Takahashi K., Ioka K., 2021, MNRAS, 501, 5746
Takami H., Nozawa T., Ioka K., 2014, ApJ, 789, L6

Tanaka M., et al., 2020, MNRAS, 496, 1369
Tanaka S. J., Takahara F., 2013, MNRAS, 429, 2945
Tanaka M., Maeda K., Mazzali P. A., Kawabata K.S., Nomoto K., 2017, ApJ, 837, 105
Tanvir N. R., Levan A. J., Fruchter A. S., Hjorth J., Hounsell R. A., Wiersema K., Tunnicliffe R. L., 2013, Nature, 500, 547
Temim T. et al., 2006, AJ, 132, 1610
Troja E. et al., 2007, ApJ, 665, 599
Troja E. et al., 2022, MNRAS, 510, 1902
Uhm Z. L., Zhang B., Hascoët R., Daigne F., Mochkovitch R., Park Il H., 2012, ApJ, 761, 147
Villar V. A. et al., 2017, ApJ, 851, L21
Vlasov A. D., Metzger B. D., Lippuner J., Roberts L. F., Thompson T. A., 2017, MNRAS, 468, 1522
Vurm I., Metzger B. D., 2021, ApJ, 917, 77
Wallace W. F., Sarin N., 2024, preprint (arXiv:2409.07539)
Wang X., Huang Y. F., Kong S. W., 2009, A&A, 505, 1213
Wang X.-G., Zhang B., Liang E.-W. et al., 2015, ApJS, 219, 9
Wang L. J., Yu H., Liu L. D. et al., 2017, ApJ, 837, 128
West S. L., Lunnan R., Omand C. M. B. et al., 2023, A&A, 670, A7
Xie X., Zrake J., MacFadyen A., 2018, ApJ, 863, 58
Xu D. et al., 2021, GRB Circ., 30357, 1
Yang B. et al., 2015, Nature Commun., 6, 7323
Yu Y.-W., Zhang B., Gao H., 2013, ApJ, 776, L40
Yu Y.-W., Liu L.-D., Dai Z.-G., 2018, ApJ, 861, 114
Zhang B., 2018, The Physics of Gamma-Ray Bursts. Cambridge University Press
Zhang W., MacFadyen A., 2009, ApJ, 698, 1261
Zhang B., Mészáros P., 2002, ApJ, 566, 712
Zhang B., Mészáros P., 2004, Int. J. Mod. Phys. A, 19, 2385
Zhang B., Fan Y. Z., Dyks J., Kobayashi S., Mészáros P., Burrows D. N., Nousek J. A., Gehrels N., 2006, ApJ, 642, 354
Zhou H., Jin Z.-P., Covino S., Lei L., An Y., Gong H.-Y., Fan Y.-Z., Wei D.-M., 2023, ApJ, 943, 104
Zhu Y.-M., Zhou H., Wang Y., Liao N.-H., Jin Z.-P., Wei D.-M., 2023, MNRAS, 521, 269

APPENDIX A: OVERVIEW OF THE PWN MODEL

This model is based on the analytic scalings presented in Murase et al. (2021). The dynamics for the model are calculated in the same way as Sarin et al. (2022) and Omand & Sarin (2024); see those papers for details.

A1 Emission

The spin-down luminosity of the PWN can be given by the equation (Lasky et al. 2017)

$$L_{\rm SD}(t) = L_0 \left(1 + \frac{t}{t_{\rm SD}}\right)^{\frac{1+n}{1-n}}, \tag{A1}$$

where L_0 is the initial PWN luminosity, $t_{\rm SD}$ is the spin-down time, and n is the pulsar breaking index. Equation A1 can be substituted for other spin-down formalisms, such as in Sarin et al. (2022). The magnetic field of the PWN is estimated as

$$B_{\rm neb} \approx \sqrt{\frac{6\epsilon_{\rm B}}{R_{\rm ej}^3} \int L_{\rm SD} dt}, \tag{A2}$$

where $\epsilon_{\rm B}$ is the fraction of spin-down energy carried in the magnetic field of the PWN. This value is usually around 0.003 for Galactic PWNe (Kennel & Coroniti 1984; Tanaka et al. 2020, Tanaka & Takahara 2013), but has been inferred to be lower in some superluminous SNe (Vurm & Metzger 2021). The characteristic synchrotron frequency, where νF_ν peaks, is

$$\nu_b \approx \frac{3}{4\pi} \gamma_b^2 \frac{e B_{\rm neb}}{m_e c}, \tag{A3}$$

where γ_b is the electron injection Lorentz factor, usually taken to be $10^4 - 10^7$ for Galactic PWNe (Tanaka & Takahara 2013). This is true if ν_b is lower than the maximum synchrotron frequency $\nu_M \sim 3.8 \times 10^{22}$ Hz. F_ν in the fast cooling limit is

$$F_\nu = F_{\nu 0} \left(\frac{\nu}{\nu_0}\right)^{1-\beta_l} = \frac{\epsilon_e L_{\rm SD}}{8\pi d^2 \nu_0 \mathcal{R}_0 (1 + Y_{\rm IC})} \left(\frac{\nu}{\nu_0}\right)^{1-\beta_l}, \tag{A4}$$

for $l = 1(2)$ when $\nu < (>)\nu_0$, where $\nu_0 = \min[\nu_b, \nu_M]$ is the peak of the νF_ν spectrum, $\epsilon_e \approx 1 - \epsilon_B$ is the fraction of spin-down energy carried by non-thermal leptons,

$$\mathcal{R}_0 = \frac{1}{2 - q_1} - \frac{1}{2 - q_2} \tag{A5}$$

is the bolometric normalization factor, $Y_{\rm IC}$ is the Compton Y parameter (which we assume to be 0, since we only model a synchrotron nebula), and d is the distance to the source. The photon indices β_1 and β_2 introduced by $F_\nu \propto \nu^{1-\beta_n}$ are $\beta_1 = \max[3/2, (2 + q_1)/2]$ and $\beta_2 = (2 + q_2)/2$, where $q_1 < 2$ and $q_2 > 2$ are the low and high energy spectral indices of the non-thermal leptons.

Table A1. The parameters and default priors implemented for this model. Priors are either uniform (U) or log-uniform (L).

Parameter	Definition	Units	Prior/value
$M_{\rm ej}$	Ejecta mass	$M_\odot$	L [0.1, 100]
L_0	Initial spin-down luminosity	erg s^{-1}	L [10^{40}, 10^{50}]
$t_{\rm SD}$	Spin-down time	s	L [10^2, 10^8]
n	Magnetar braking index		U [1.5, 10]
$\epsilon_{\rm B}$	Magnetic field partition parameter		L [10^{-7}, 1]
γ_b	Electron injection Lorentz factor		L [10^2, 10^7]
$E_{\rm K}$	Initial kinetic energy	erg	10^{51}
κ	Ejecta optical opacity	cm^2 g^{-1}	0.1
κ_γ	Ejecta gamma-ray opacity	cm^2 g^{-1}	0.01
q_1	Low energy spectral index		1.5
q_2	High energy spectral index		2.5
$\bar{Z}$	Ejecta average atomic number		8
Y_e	Ejecta electron fraction		0.5
$Y_{\rm fe}$	Ejecta free electron fraction		0.0625

A2 Absorption

PWN emission can be subject to various absorption processes depending on the frequency of the emission. At radio frequencies, SSA and FFA are the main processes. At 10 eV–10 keV bands, the dominant process is photoelectric (bound-free) absorption. At 10 keV–10 MeV bands, the dominant process is Compton scattering. Other bands have different processes, such as Bethe–Heitler pair production for >10 MeV bands and bound-bound absorption in the optical/infrared bands (Kashiyama et al. 2016), but we only include absorption processes in the radio and 10 eV–10 MeV bands.

The SSA frequency can be estimated by (Murase et al. 2021)

$$\pi \frac{R_{\rm ej}^2}{d^2} 2kT_{\rm ssa} \frac{\nu_{\rm ssa}^2}{c^2} = F_{\nu 0} \left(\frac{\nu_{\rm ssa}}{\nu_0} \right)^{1-\beta_1}, \tag{A6}$$

where

$$T_{\rm ssa} = \frac{1}{3k} \left(\frac{4\pi m_e c \nu_{\rm ssa}}{3eB_{\rm neb}} \right)^{1/2} m_e c^2 \tag{A7}$$

is the brightness temperature at $\nu_{\rm ssa}$. This approximately gives

$$\nu_{\rm ssa} \approx \left(\frac{3^{3/2} e^{1/2} B_{\rm neb}^{1/2} F_{\nu 0} \nu_0^{\beta_1 - 1} d^2}{4\pi^{3/2} m_e^{3/2} c^{1/2} R_{\rm ej}^2} \right)^{\frac{2}{2\beta_1 + 3}}. \tag{A8}$$

The optical depth for free-free absorption is (Lang 1999; Murase, Kashiyama & Mészáros 2017)

$$\tau_{\rm ff} \approx 8.4 \times 10^{-28} n_e^2 R_{\rm ej} \bar{Z}^2 \left(\frac{\nu}{10\ {\rm GHz}} \right)^{-2.1}, \tag{A9}$$

where

$$n_e = \frac{3}{4\pi R_{\rm ej}^3} \frac{M_{\rm ej} Y_{\rm fe}}{m_p} \tag{A10}$$

is the electron density, $\bar{Z}$ is the average atomic number of the ejected material, and

$$Y_{\rm fe} \equiv \frac{n_{\rm fe}}{n_p + n_n} \tag{A11}$$

is the free electron fraction, with $n_{\rm fe}$ being the free electron density.

The optical depths for optical and x-ray absorption can be generally written as $\tau = \kappa \rho_{\rm ej} R_{\rm ej}$ for opacity κ, where the opacity for photoelectric absorption is approximated as (Murase et al. 2015; Kashiyama et al. 2016)

$$\kappa_{\rm pe} = 11 \left(\frac{\bar{Z}}{10} \right)^3 \left(\frac{h\nu}{10\ {\rm keV}} \right)^{-3}\ {\rm cm^2 g^{-1}} \tag{A12}$$

and for Compton scattering as (Murase et al. 2015)

$$\kappa_{\rm comp} = \frac{\sigma_{\rm KN} Y_e}{m_p}, \tag{A13}$$

where $\sigma_{\rm KN}$ is the Klein–Nishina cross-section (Klein & Nishina 1929) and Y_e is the electron fraction of the ejecta. The optical opacity is generally taken to be free parameter in most light curve models (e.g. Arnett 1982; Villar et al. 2017), and we adopt the same treatment here.

A3 Parameters and default priors

This model is implemented as the PWN model in GENERAL_SYNCHROTRON_MODELS within REDBACK. Along with the parameters that can freely vary during inference, there are a number of parameters that have default values consistent with an SN, but that can be changed if the user wants to model a KN. These can also be given priors and marginalized over if needed. The parameter κ_γ here is only used in the dynamics on the SN, not in the calculation of the PWN spectrum. A summary of the parameters and priors is given in Table A1.

APPENDIX B: POSTERIOR FOR INFERENCE ON A SIMULATED LIGHT CURVE

The posterior for the fit done in Section 3.2 is shown in Fig. B1.

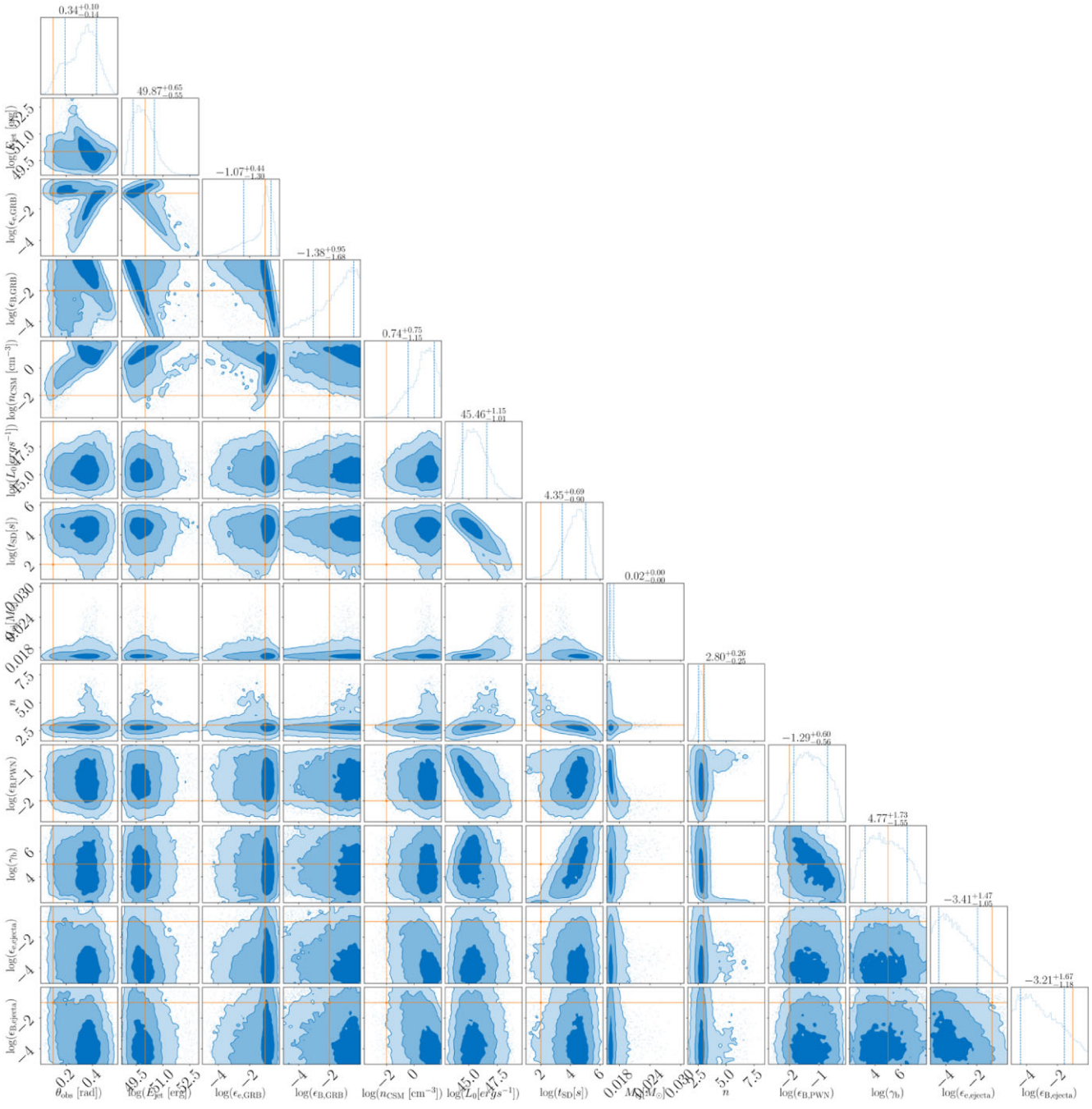

Figure B1. The parameter posterior inferred for the simulated KN/SGRB. The orange dots and lines indicate the injected parameters.

This paper has been typeset from a TEX/LATEX file prepared by the author.